ELSEVIER

Mechanics of Materials 31 (1999) 765–786

MECHANICS OF MATERIALS

www.elsevier.com/locate/mechmat

On transport in stochastic, heterogeneous fibrous domains

X. Cheng, A.M. Sastry *

Department of Mechanical Engineering and Applied Mechanics, University of Michigan, 2350 Hayward, 2250 G.G. Brown, Ann Arbor, MI 48109-2125, USA

Received 27 January 1999; received in revised form 5 April 1999

Abstract

Design of porous, fibrous structures is needed in a number of important technological applications. We focus on material parameters relevant to conductive substrates in advanced battery systems, though similar microstructures arise in many engineered and natural materials. The conductivities of stochastically-generated fiber networks are examined, with an emphasis on the variance in observed properties based on material variability, scale dependence of solution, and the occurrence and strength of singularities encountered in solution of the high contrast cases. We show that rigorous bounds on material behavior are too wide to be practically useful in these stochastic networks, and that material property variance is reasonably predicted by use of our stochastic finite element-fiber network approach. We further show that the boundary conditions employed in solution of Laplace's equation in heterogeneous domains critically affects solution, and suggest guidelines for solution for a general network based on sharpness of interior angles. Degree of contrast in material phases' properties are also discussed in how they affect the simplicity of the approach which can be taken in modeling real networks. We further assess the scale-dependence of our calculations. Finally, we demonstrate that the stochastic finite element/stochastic network solutions are robust, and are able to accurately predict both effective conductivity, and variance in conductivity, in these materials.

1. Introduction

Transport in real, heterogeneous microstructures depends strongly on the shape, orientation and property contrast in the material phases. The central goal of the current work is to tailor properties of fibrous materials through selection of microstructure. The microstructures of interest can be controlled only within some statistical bounds, which we identify at the outset. These bounds are dictated by cost-effectiveness in production of fibrous materials – while some material parameters can be controlled easily and inexpensively, others (e.g., orientation) come at substantial cost penalty.

The class of materials under investigation encompasses the materials shown in Fig. 1. Briefly, we specify that such materials are comprised of fibers randomly arranged in 2D, with known aspect ratio, staple length (i.e., original fiber length) and orientation. Since we are interested in the effect of local microstructure on material properties rather than developing very general bounds on properties, we focus on material parameters relevant to a particular technological application-conductive substrates in advanced battery systems (Fig. 1b). Reduced conductivity in these substrates limits both cell capacity and cell lifetime. As such, design of the microstructure of these materials is critical to efficient, high-capacity operation of

* Corresponding author. Tel.: +1-734-764-3061; fax: +1-734-647-3170.

E-mail address: amsastry@umich.edu (A.M. Sastry)

0167-6636/99/$ - see front matter
PII: S0167-6636(99)00031-9

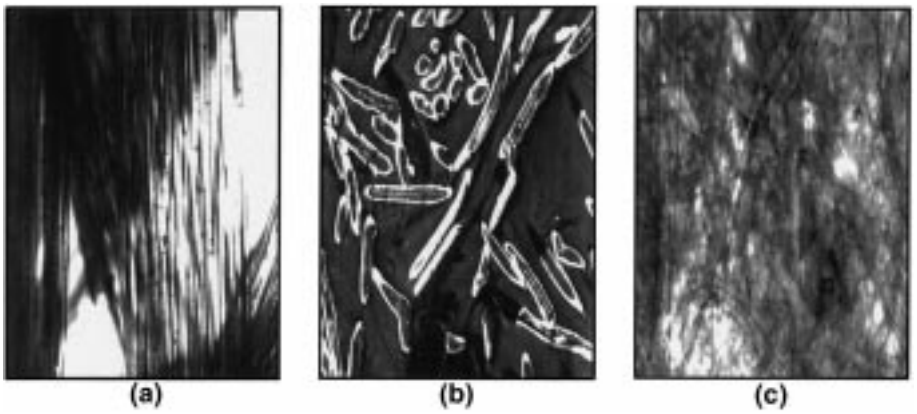

Fig. 1. Material microstructures of interest. (a) Randomly arranged (continuous strand mat) glass fibers for use in reinforcement of polymeric composites. (b) Randomly arranged nickel fibers in a Ni/MH hydride positive plate substrate. (c) Randomly arranged cellulose fibers in newspaper.

modern electrochemical cells (e.g., Ferrando et al., 1984; Tatarchuk, 1994).

Two general classes of interest have been studied both theoretically and experimentally by the authors: high-contrast networks (Cheng et al., 1999a, b; Wang et al., 1999; Sastry et al., 1998a, b) in which all but one phase are considered to have negligibly small conductivity; and medium to low contrast networks (the present work). We have developed a network generation technique which involves placing stochastically-arranged fibers in a periodic unit cell (Fig. 2a–c). In many applications, a fibrous network is immersed or encased in a conductive material during application, which alters the strategy for materials design. A two-fold strategy motivates the present work:

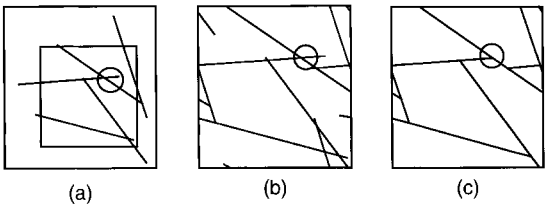

Fig. 2. Network generation technique, for 1D fibers. (a) Fibers are placed according to network statistics, in a unit cell; (b) periodic boundary conditions are enforced, preserving volume fraction specified at the outset for the cell; and (c) non-conductive ends are removed. The circled end demonstrated the technique: fiber ends are removed in this approach.

1. *Technological strategy*. In Ni/MH batteries, conductive substrates such as those shown in Fig. 1b are filled with active material, and then immersed in conductive electrolyte. Analysis must allow comparison between moderate increase in conductivity of other phases (active material and/or electrolyte) and addition of more conductive fibrous mass to attain desired conductivity in the composite.
2. *Solution strategy*. In general, we wish to identify the magnitude of contrast required for use of simpler approaches (series–parallel resistor models), rather than full finite element solution of effective conductivity. We assume that simulations are scale-dependent and also microstructure-dependent.

Some statistical work accounting for material irregularities has been previously performed for high-contrast networks. Kirkpatrick (1973) studied site and bond percolation using a resistor network, and pointed out the importance of percolation threshold. McLachlan (1988) introduced a more general effective-media equation for binary conductivity media. Ostoja-Starzewski et al. (1994, 1996) developed network techniques to simulate effective properties of generalized composites. Nonetheless, it is very difficult to calculate the percolation threshold, critical in assessing transport properties, for most realistic microstructures. The few published values of percolation

threshold are only for specifically arranged spheres, circles and networks. Furthermore, rigid theoretical bounds on transport behavior are often too wide to be practically useful. The series and parallel bounds are given by

$$K_{\text{eff}} = \frac{k_1 k_2}{k_1(1-f) + f k_2} \tag{1}$$

and

$$K_{\text{eff}} = f k_1 + (1-f) k_2 \tag{2}$$

respectively, where f is the volume fraction of the phase with conductivity k_1. These relations return an upper bound of $K_{\text{eff}} = f k_1$ (parallel bound, with $k_2 = 0$) and a trivial lower bound ($K_{\text{eff}} = 0$) when the conductivity of one of the two phases is negligible. While these bounds are rigorous for transport in high-contrast materials (Borcea and Papanicolaou, 1997), they are generally be useful in most practical materials selection applications.

Work by the present authors has focused on developing a technique for realistic network generation (Cheng et al., 1999a, b; Sastry et al., 1998a, b) and methodologies for simplified simulation approaches for network conductivities, as compared with exact resistor network calculations (Cheng et al., 1999b). In this paper we continue this work, and assess the applicability of the resistor network model to materials of moderate contrast, and also discuss appropriate scales of simulation. We are particularly interested in the variance in conductivity, and how it varies under physically realistic ranges of network parameters. This is in contrast to related, classic work in micromechanics, which typically has sought to either bound properties (e.g., Hashin and Shtrikman, 1962) or to calculate deterministically a single effective transport coefficient in a model microstructure (for an excellent review of prior classic work in electrostatics, see Meredith and Tobias, 1962; or McLachlan et al., 1990).

We are particularly interested in the effect of scale. The connectivities, and thus the calculated conductivities of our networks are scale-dependent, as are all such simulations in heterogeneous domains, where the scales of the heterogeneities and simulations are sufficiently close. We observe that variance in observed conductivity depends strongly, as one would expect, on "window size", or size of the region simulated. Rather than attempt to develop very broad scaling laws for all possible microstructures in stochastic fibrous networks, we focus attention on a particular range of parameters relevant to battery substrates. Some results of validating experiments are also presented. Future work will focus on further validation with experiments, and applications of the simulation techniques to other ranges of microstructural shapes and sizes.

Finally, singularities inherent in potential fields in heterogeneous media containing sharp boundaries present computational challenges, and can be dealt with either by adaptive remeshing of domains, or selective smoothing of microstructures. This topic is also addressed in the present work.

2. Stochastic network generation and solution techniques

Motivated by the moderate variability exhibited by most of the fibrous materials of interest, we use either normal distributions, uniform distributions or single parameters in our network generation for six network variables: fiber volume fraction, fiber orientation distribution, fiber length distribution, fiber centerpoint (both in x and y directions) and fiber aspect ratio. A number of single-parameter distributions have been suggested for describing orientation in fibrous materials (e.g., Mardia, 1972; Schulgasser, 1985). Such single parameter distribution functions can be useful for establishing bounds on behavior. However, they often fail to capture the distribution of microstructures in a real material. Fig. 3a gives a histogram of sample data on measured fiber diameter (from image analysis) in the battery substrates of interest with a fitted normal distribution; Fig. 3b gives a histogram of fiber length data (from image analysis of substrates) with a fitted gamma distribution, given by

$$f(x) = \begin{cases} \dfrac{x^{a-1}\mathrm{e}^{-(x/b)}}{\Gamma(a)b^a} & x \geqslant 0, \quad a > 0,\ b > 0, \\ 0 & x < 0 \end{cases} \tag{3}$$

in general form. Fig. 3c shows a fit of one-parameter wrapped Cauchy distribution to the

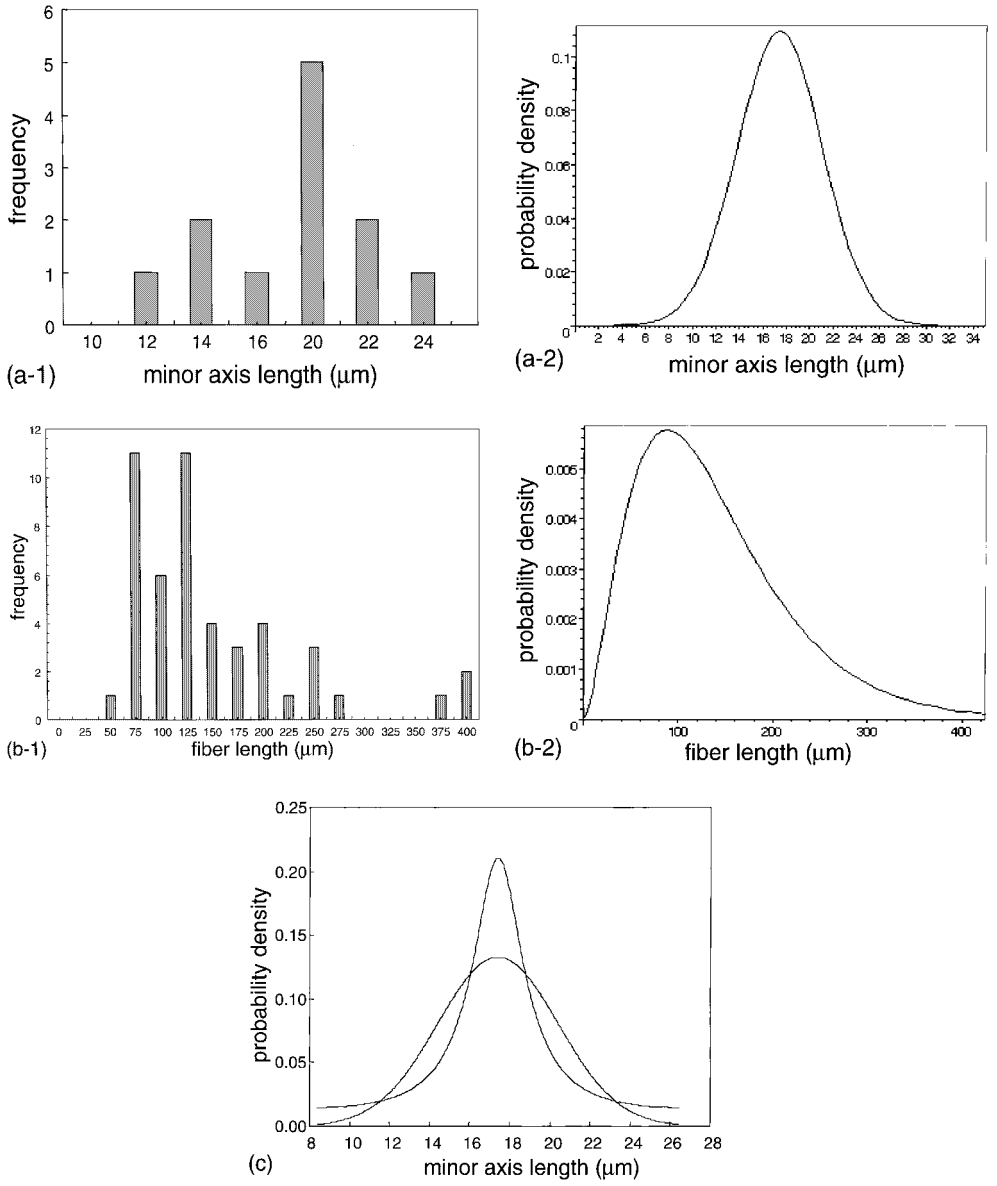

Fig. 3. Real network data compared with various statistical distributions, including: (a) Histogram of data generated from image analysis of nickel substrate material (National Standard AFS substrate material, 95% porosity). A normal distribution function is fitted to the data, with mean and variance of 17.420 and 3.645 μm, respectively. (b) Histogram of fiber length data generated from image analysis of nickel substrate material (National Standard Fibrex substrate material, 82% porosity). A fit is shown using a Gamma distribution with parameters $\alpha = 2.761$, $\beta = 49.848$ ($\mu = 137.634$ μm and $\alpha = 82.830$ μm), respectively. (c) Comparison of the Wrapped Cauchy distribution (dashed line) ($\rho = 0.5820$) with the normal distribution of fiber diameters in Fig. 3a.

normally distributed fiber diameters of Fig. 3a, with the distribution function given by

$$f(\theta) = \frac{1-\rho^2}{\pi(1+\rho^2-2\rho\cos 2\theta)} \tag{4}$$

in general form, where ρ is a measure of dispersion, and the mean value is $\cos 2\theta$. Better agreement could of course be obtained for data more closely clustered about the mean, or uniformly

distributed ($\rho = 0$), but the distributions we encounter in substrate materials, at least, are poorly fitted by these approaches.

Particle shape distributions are also bimodal in many types of stochastic fibrous structures, with long fibers interspersed with particles (as is the case in several types of battery substrates). Using the basic algorithm we developed, described in the flow chart of Fig. 4, all of these microstructures can be numerically generated. In the results reported here, uniform (random) distributions for fiber orientation (0°–90°), and x- and y-location of centerpoint were used. The effects of moderate orientation (normal distributions, with specified mean and standard deviation in orientation for a number of fibers in a given simulation) are addressed elsewhere (Cheng et al., 1999b).

Two approaches are used to evaluate the conductivity of the stochastic networks generated. The first technique assumes only a single conductive phase (i.e., high contrast composite), and involves conversion of a randomly-laid 2D fibrous network into an equivalent series–parallel resistor network (as in Cheng et al., 1999b). The second technique involves generation of a two-phase domain, with high aspect-ratio ellipses representing fibers in the network, and non-zero conductivity in both phases. The techniques are described below, in order.

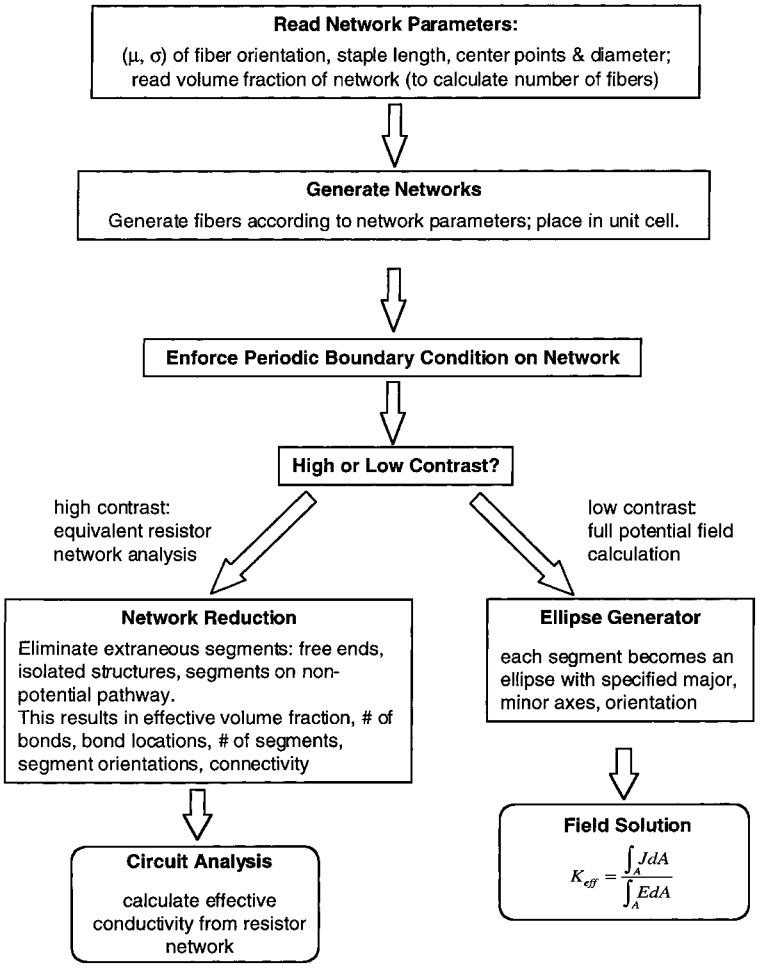

Fig. 4. Flow chart of network generation for the two approaches.

2.1. High contrast networks: methodology

For the high contrast case, fibers are placed in the unit cell according to the appropriate distribution functions. This produces a point-bonded network comprised of fiber segments as shown in Fig. 2. In this case, each fiber segment is modeled as a resistor, with resistance proportional to segment length, as

$$R_i = \frac{\rho_f L_i}{A_i} = \frac{L_i}{A_i k_f}, \tag{5}$$

where A_i is the cross-section area of ith fiber, L_i the length of ith fiber, ρ_f the resistivity of ith fiber and k_f is the conductivity of the fiber material.

Thus, the stochastic arrays to analytically tractable series–parallel resistor networks, as shown in Fig. 5. Generation of such 2D networks from 1D fibers allows examination of connectivity of networks, in addition to calculation of their effective conductivity (e.g., Sastry et al., 1998a). But there are several significant departures from real network geometries in this model, including the facts that "overlapping" domains are ignored in terms of how they affect volume fraction and connectivity; contact resistivity is ignored; and examination of properties in materials containing phases of relatively low contrast is not possible.

2.2. Lower contrast networks: methodology

Determination of the full potential field is required in order to obtain the effective conductivity of a medium in which there is more than one-phase of non-negligible conductivity. Effective conductivity follows from potential field solution as

$$K_{\text{eff}} = \frac{\int_A J \, dA}{\int_A E \, dA}, \tag{6}$$

where J is the current density field, E the electrical intensity field and A is the surface area of problem domain.

Fields E and J are calculated numerically (in this case using a commercial finite element package, Maxwell 2D) and surface integrations are performed through the entire problem domain to obtain K_{eff}. Fig. 6 demonstrates the potential field information generated by the FE approach. The boundary conditions shown allow periodic cells to be generated, as well as allowing calculation of effective conductivity as described above.

Fiber geometry employed. The real fibers of interest are essentially cylindrical rods (Fig. 7a). For finite element analysis of the irregular, heterogeneous domain of a network of such fibers, however, we represent fibers as 2D ellipses, rather than rectangles (Fig. 7b) with thickness D, the fiber diameter. We take this approach for two reasons.

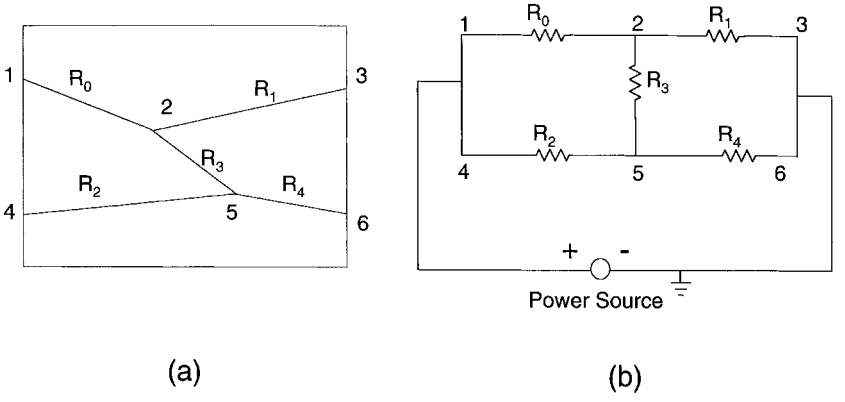

Fig. 5. Conversion of a stochastic fibrous network comprised of 1D fibers into an equivalent series–parallel network, for exact calculation of conductivity.

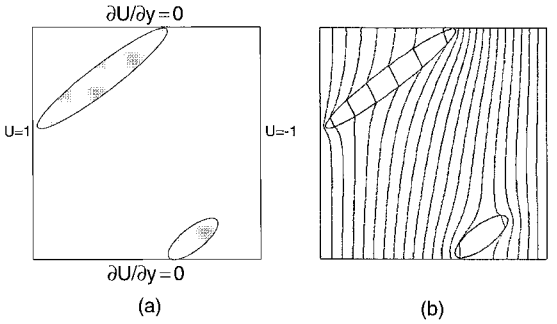

Fig. 6. The potential field generated in an array of stochastically-oriented ellipses (volume fraction = 7.854%; staple length = 1.0; diameter = 0.1), with applied potential boundary conditions on opposite faces, and flux boundary conditions on the remaining faces.

First, we wish to smooth edges as much as possible. We cannot eliminate the "ends" of connected fibers as in the high contrast case, since we seek solution for the full potential field; moreover, these ends comprise a significant proportion of the network. By representing fibers as ellipses, we eliminate singularities due to the ends, though we still must contend with singularities arising due to fiber–fiber contacts. Second, we wish to preserve the ability to smoothly handle domains containing distributions of fibers and particles, which we do (see Fig. 7c) via representation of fibers as high aspect ratio ellipses ($a/b \ll 1$), and particles as circles ($a/b = 1$).

In selection of an equivalent 3D object with elliptical cross-section to approximate a circular cylinder (Fig. 7a, b), we can elect to match either cross-sectional area in the 2D projection, or match volumes of the objects in 3D. In the first case (Fig. 7c) we would scale the width of the ellipse as D' where $D' = 4D/\pi$. This results in a 2D ellipse with area $ab = \pi D'L/4 = DL$, which is equal to the area of the projection of the circular cylinder. If we use this approach, however, we develop errors in calculations of the volume fraction assuming a thickness of a single fiber diameter, since the two volume fractions are

$$f' = \frac{D\sum_{i=1}^{N} L_i}{L_u^2} \tag{7}$$

for the equivalent elliptical geometry, and

$$f = \frac{\sum_{i=1}^{N} \pi D^2 L_i}{4L_u^2 D} = \frac{\pi D \sum_{i=1}^{N} L_i}{4L_u^2} \tag{8}$$

for the circular cylinder geometry, which are approximately 21.5% in disagreement with one another.

The second approach, which we adopt here, matches volume fractions of the objects in 3D, as shown in Fig. 7d. Using this approach, we

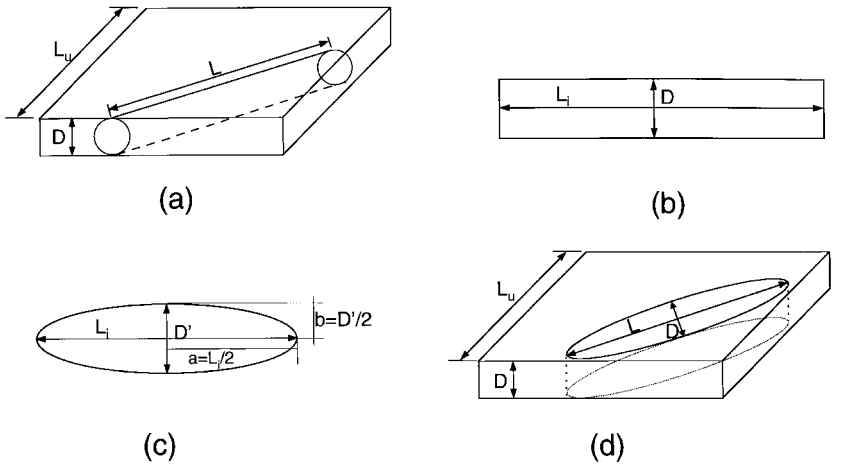

Fig. 7. Fiber representations under different assumptions of equivalent area versus volume. (a) Cross-section of fiber rod of length L_i, diameter D. (b) Rectangle with equal cross-sectional area. (c) 2D ellipse with equal cross-sectional area to that projected by the cylindrical fiber in 2D. (d) Elliptical cylinder representation, having equal volume to the circular cylindrical fiber.

approximate a cylindrical fiber as an elliptical cylinder, with cross-sectional geometry as shown. In this case, the volumes match, as

$$f = \frac{\sum_{i=1}^{N} \pi abL_i}{L_u^2 D} = \frac{\sum_{i=1}^{N} \pi (D/2)(L_i/2)D}{L_u^2 D} = \frac{\pi D \sum_{i=1}^{N} L_i}{4L_u^2}. \quad (9)$$

Demarcation of problem domain. Even in heterogeneous domains of only moderate contrast, contact of the more conductive material with an edge where a potential boundary condition is applied can change the solution for the potential field dramatically if there is a fully connected conductive path to the adjacent boundary (percolation). Experimentally, this would translate as placement of an electrode on a fiber rather than a pore, or in less-conductive electrolyte, and obtaining a dramatically different measurement of conductivity of the composite.

In our approach, the problem domain was defined as the four edges of the cell (not, any longer, a ''unit'' cell) tangential to the ellipses (Fig. 8a) marking the maximum and minimum values x and y directions respectively. Calculation of the location of these edges proceeded as follows.

With a general definition of an ellipse in x–y space as:

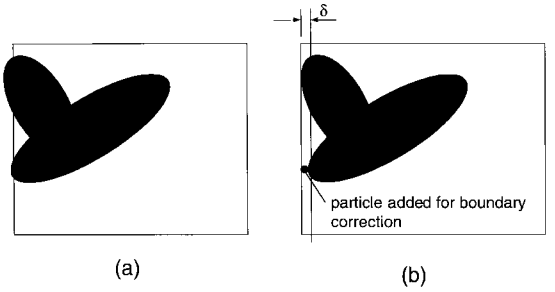

Fig. 8. Geometric descriptors of a generalized ellipse in 2D, and consequence of edge corrections in generated networks. (a) Original configuration. (b) Approach and geometry in ''corrected'' edge, whereby small particles, of the same conductivity as the other particles, are added to elliptical elements who are displaced away from the boundary when boundary is set at most outlying ellipse. (c) Plot of normalized conductivity in edge-corrected geometries, for 10% volume fraction, demonstrating the small effect on conductivity of the necessary shifts.

$$Ax^2 + Bxy + Cy^2 + Dx + Ey + F = 0, \quad (10)$$

where:

$$A = 4m^2 - 4(x_{f2} - x_{f1})^2,$$
$$B = -8(x_{f2} - x_{f1})(y_{f2} - y_{f1}),$$
$$C = 4m^2 - 4(y_{f2} - y_{f1})^2,$$
$$D = -4(x_{f2} - x_{f1})\left(x_{f1}^2 + y_{f1}^2 - x_{f2}^2 - y_{f2}^2 - m^2\right) - 8m^2 x_{f2},$$
$$E = -4(y_{f2} - y_{f1})\left(x_{f1}^2 + y_{f1}^2 - x_{f2}^2 - y_{f2}^2 - m^2\right) - 8m^2 y_{f2},$$
$$F = 4m^2 x_{f2}^2 + 4m^2 y_{f2}^2 - \left(x_{f1}^2 + y_{f1}^2 - x_{f2}^2 - y_{f2}^2 - m^2\right)^2,$$
$$m = \sqrt{(x_{11} - x_{12})^2 + (y_{11} - y_{12})^2}.$$

Eq. (10) can be solved for x as

$$x = \frac{-D - By \pm \sqrt{D^2 + 2DBy + B^2y^2 - 4AEy - 4AF - 4ACy^2}}{2A}. \quad (11)$$

Setting

$$\frac{dx}{dy} = 0 \quad (12)$$

results in:

$$y = \frac{-2AEC + DBC \pm \sqrt{D^2B^2C^2 + CB^4F - CB^3DE + CB^2AE^2 - 4AC^2FB^2}}{-CB^2 + 4AC^2} \quad (13)$$

which corresponds to the y-values at the maximum and minimum x coordinates. The same procedure may be used to find the minimum and maximum y. Writing the definition of the ellipse in terms of x, we have

$$y = \frac{-E - Bx \pm \sqrt{E^2 + 2EBx + B^2x^2 - 4CDx - 4CF - 4ACx^2}}{2C} \quad (14)$$

and for $dy/dx = 0$, we obtain

$$x = \frac{-2ACD + EBA \pm \sqrt{E^2B^2A^2 + AB^4F - AB^3ED + CB^2AD^2 - 4A^2CFB^2}}{-AB^2 + 4CA^2} \quad (15)$$

which can then be solved to determine the x-values at the maximum and minimum y coordinates.

When this procedure is carried out, the slight shifting of the boundary of the cell sometimes causes a loss of contact with one or more ellipses which initially were in contact, but did not mark the outlying bounds. In this case, small connective elements are added to these ellipses, to preserve

their connection to the boundary as in the initial network simulated (Fig. 8b).

There are three issues which must be addressed in this problem. First, the size of the "measuring device", as compared to the size of the microstructures, is critical. In an experiment (e.g., Sastry et al, 1999b), a multi-probe measurement is typically used to assess conductivity of a thin plate. In the simulations here, however, an edge was specified for application of the potential boundary condition rather than a series of points, so that this first issue does not cause immediate problems. The second issue is the geometry of contact of the conductive object with the boundary line. Simulations performed on particles for the present work indicate that the effective conductivity of a field containing a conductive particle in a low-conductivity matrix is almost entirely insensitive to contact with either the main ellipse at the edge, or an ellipse connected by a single small particle, as shown in Fig. 8c. The third issue is the truncation of ellipses by the "unit cell". This is related to the second issue; since we find that point contact was sufficient (so that there is no necessity to closely model the length of contact), we simply extend the surrounding boundaries of the cell to be tangent to any edge-overlapping ellipse at a single point.

Numerical solution in the presence of singularities. In solution of Laplace's equation in heterogeneous domains with sharp phase boundaries, several sources of singularities are encountered, including corners in the solution domain, abrupt changes in boundary data and singularities arising at material interfaces (Oh and Babuska, 1992, 1995; Babuska and Oh, 1990; Babuska et al., 1996). Adaptive finite element methods can be used in order to provide accurate solutions for problems with numerical singularities. The accuracy of h-version, the standard finite element method, is achieved by refining the mesh while the degree p of the elements is fixed and at low level, usually $p = 1, 2, 3$. The p-version entails increasing the degree of shape function p, while fixing mesh size. An h–p version employs some combination of these two. Oh and Babuska (1992, 1995) introduced the MAM (method of auxiliary mapping) to deal with domain and interface singularities. Nevertheless, the h-version remains the most popular approach due to widely-available and user-friendly commercial packages which offer iterative mesh refinement. However, for sufficiently strong singularities, this approach is unable to provide acceptable results.

In generation of physically representative stochastic fiber structures, it is nearly impossible to avoid generation of interior polygons with sharp corners formed by randomly distributed fibers. We report both the strength of the singularities typically encountered in these problems, and later, comment on the likelihood of their occurrence. Since our numerical approach was to employ a commercial code (Maxwell 2D) which used triangular elements, we restricted our strategy to such mesh refinement.

We can construct an exact (if not always explicit) solution for Laplace's equation via the general technique outlined in Appendix A, for a heterogeneous field containing discrete singularities. The solution of Laplace's equation for a single corner point in two-phase domain is used in all of the derivations that follow; it is derived in Appendix B.

The intensity of each singularity is determined by the smallest positive real number of the structural eigenvalues, λ. The magnitude of these eigenvalues guide selection of strategy in numerical solution. Oh and Babuska (1992) determined these eigenvalues for the specific microstructure shown in Fig. 9a, with boundary conditions as shown. The complexity of the generated networks in our study motivated us to investigate singularities in other model domains as well, shown as Fig. 9b and c. Fig. 9b represents the effect of clusters of fibers or particles which do not span the solution domain, but which contain sharp corners. Fig. 9c. represents the effect of fibers or particles intersecting a boundary, so that the same boundary condition applies to both sides (unlike Fig. 9a in which the intersection of the phases simultaneously marks an intersection of boundary conditions and phases).

We also investigated the effect of differences in boundary conditions on the severity of singularities. Oh and Babuska (1992) investigated the effect of flux boundary conditions on their model microstructure (shown graphically in Fig. 10a) as

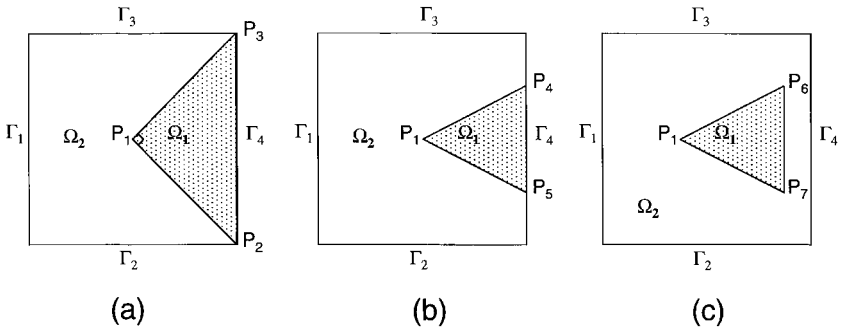

Fig. 9. Three domains investigated, to determine the magnitude of the singularities present in solution of Laplace's equation. (a) Model domain used by Oh and Babuska (1995) to investigate adaptive techniques in finite elements. (b) Model domain used to assess the effect of singularities produced by conductive particles in contact with an edge, but with only one boundary condition. (c) Model domain used to assess the singularities produced by interior clusters of particles.

$$\begin{aligned} &\partial U/\partial y = 0 \quad \text{on } \Gamma_2 \cup \Gamma_3, \\ &\partial U/\partial x = 1 \quad \text{on } \Gamma_1, \end{aligned} \tag{16}$$

$$U = 0 \quad \text{on } \Gamma_4. \tag{17}$$

We investigate potential boundary conditions (shown graphically in Fig. 10b), as

$$\partial U/\partial y = 0 \quad \text{on } \Gamma_2 \cup \Gamma_3, \tag{18}$$

$$U = \begin{cases} 1 & \text{on } \Gamma_1, \\ -1 & \text{on } \Gamma_4. \end{cases} \tag{19}$$

The boundary conditions of Fig. 10b, and Eqs. (18) and (19) allow generation of periodic domains, with calculation of effective properties proceeding from calculations such as Eq. (6).

Because of the linearity of the problems of interest (Figs. 9 and 10), we can construct solutions to each via superposition, as described in Appendix A. We first examine the singularity due to a corner in a two-phase domain, which is derived as Appendix B, and whose domain is sketched here also as Fig. 11a. The solution for the exponent λ

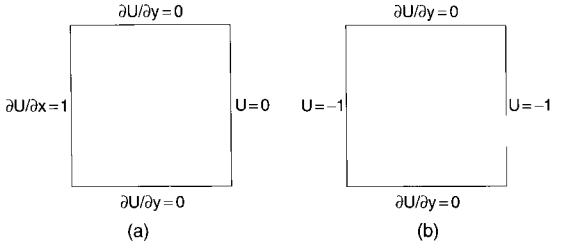

Fig. 10. Boundary conditions on model domains investigated, including (a) flux, and (b) potential boundary conditions, to allow for periodic arrangement.

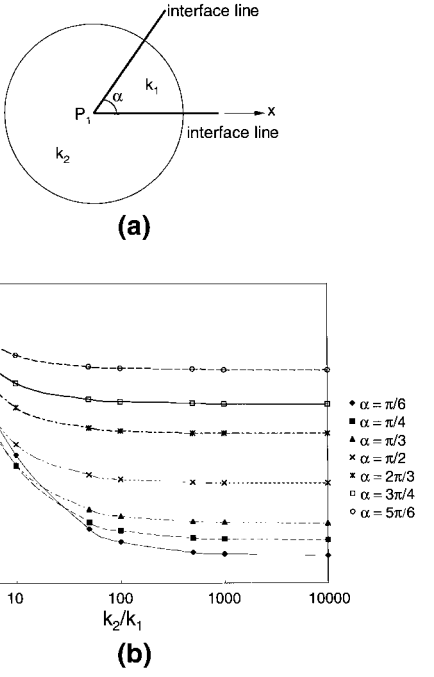

Fig. 11. (a) Schematic of a characteristic unit problem in analysis of two-phase domains, and (b) values of the associated exponents (structural eigenvalues) arising in solution for the potential field U for various levels of material contrast.

associated with the potential field about the singular point P_1, given by solution of

$$\begin{aligned} & k_2k_1 \sin(2\lambda_1\alpha) \sin(2\lambda_1\pi) \\ & - 2k_2k_1 \cos^2(\lambda_1\alpha) \cos(2\lambda_1\pi) \\ & + \frac{1}{2}k_2^2 \sin(2\lambda_1\alpha) \sin(2\lambda_1\pi) + 2k_2k_1 \\ & - k_2^2 \cos(2\lambda_1\pi) + k_2^2 \cos^2(\lambda_1\alpha) \cos(2\lambda_1\pi) \\ & + \frac{1}{2}k_1^2 \sin(2\lambda_1\alpha) \sin(2\lambda_1\pi) - k_1^2 \cos(2\lambda_1\pi) \\ & + k_1^2 \cos(2\lambda_1\pi) \cos^2(\lambda_1\alpha) = 0 \end{aligned} \tag{20}$$

does not depend on boundary conditions. Rather, it is a function of geometry and phase contrast only. Fig. 11b shows the dependence of the exponent (strength of the singularity) with phase contrast, for various interior angles α. Because this solution is not dependent upon exterior boundary conditions, the values of these singularities describe those encountered at P_1 in Fig. 9a–c, and at P_6 and P_7 in Fig. 9c.

We can similarly construct the solution about the remaining key points. We note that points P_2 and P_3 are reflection points, so we carry out a similar technique as in Appendix B, in developing a solution for the exponent λ_3 associated with the potential field about the singular point P_3 only. In this case, the solution is dependent upon exterior boundary conditions (i.e., such as those in Fig. 10a versus Fig. 10b). We first develop a relation for the exponent λ_3 with boundary conditions as in Fig. 10a, with a general domain representing these boundary conditions shown as Fig. 12a. Fig. 12b gives the values of this exponent for a range of phase contrasts, for several interior angles ϕ, obtained by solution of

$$\begin{aligned} & k_2 \sin(\phi\lambda_3/2) \cos^2(2\lambda_3\pi) \\ & - k_2 \sin(\phi\lambda_3/2) \cos^2(2\pi\lambda_3 - \phi\lambda_3/2) \\ & + \frac{1}{2}k_1 \cos(\phi\lambda_3/2) \sin(4\pi\lambda_3 - \phi\lambda_3) \\ & + \frac{1}{2}k_1 \cos(\phi\lambda_3/2) \sin(4\pi\lambda_3) = 0 \end{aligned} \tag{21}$$

which yields the explicit relation,

$$\lambda_3 = 2\frac{\arctan(\sqrt{k_1k_2}/k_2)}{\phi}. \tag{22}$$

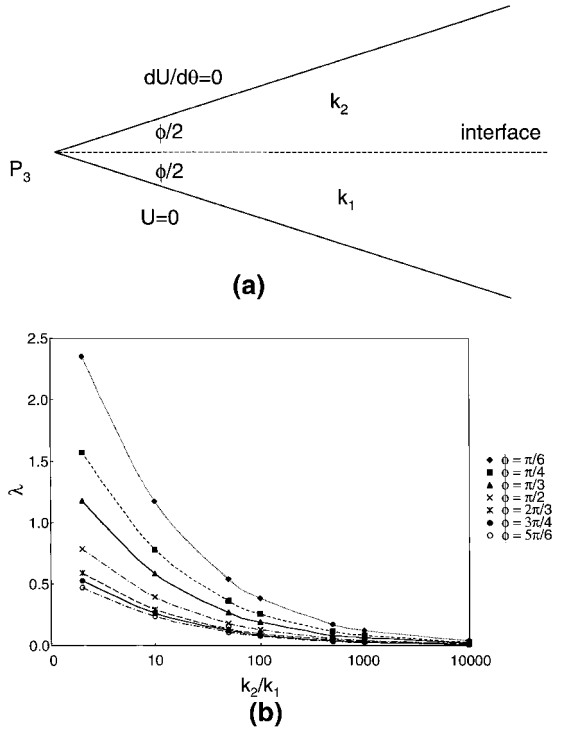

Fig. 12. (a) Schematic of a constituent solution for a model domain: solution for the structural eigenvalue in the potential field around singular point P_3 (see Fig. 9a, with boundary conditions as in Fig. 10a), and (b) values of the associated exponents for various values ϕ, over a range of volume fractions.

For the corresponding point using the boundary conditions of Fig. 10b, we solve the generalized problem of Fig. 13a, solving

$$\begin{aligned} & k_2 \sin(\gamma\lambda_3/2) \cos(2\pi\lambda_3 - \gamma\lambda_3/2) \\ & - k_1 \cos(\gamma\lambda_3/2) \sin(2\pi\lambda_3) \\ & - k_1 \cos(\gamma\lambda_3/2) \sin(2\pi\lambda_3 - \gamma\lambda_3/2) \\ & - k_2 \sin(\gamma\lambda_3/2) \cos(2\pi\lambda_3) = 0 \end{aligned} \tag{23}$$

to obtain

$$\lambda_3 = 2\frac{\arctan(\sqrt{2k_1k_2 + k_1^2}/k_2)}{\gamma} \tag{24}$$

which is plotted over similar parameters in Fig. 13b.

The only remaining points whose associated singularities must be found are points P_4 and P_5 in Fig. 9b (recalling that points P_6 and P_7 in Fig. 9c

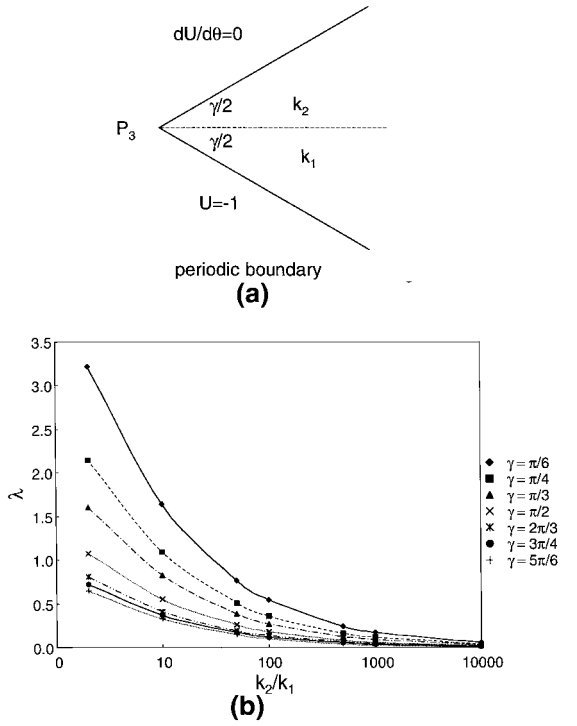

Fig. 13. (a) Schematic of a constituent solution for a model domain: solution for the structural eigenvalue in the potential field around singular point P_4 (see Fig. 9b, with boundary conditions as in Fig. 10a), and (b) values of the associated exponents for various values γ, over a range of volume fractions.

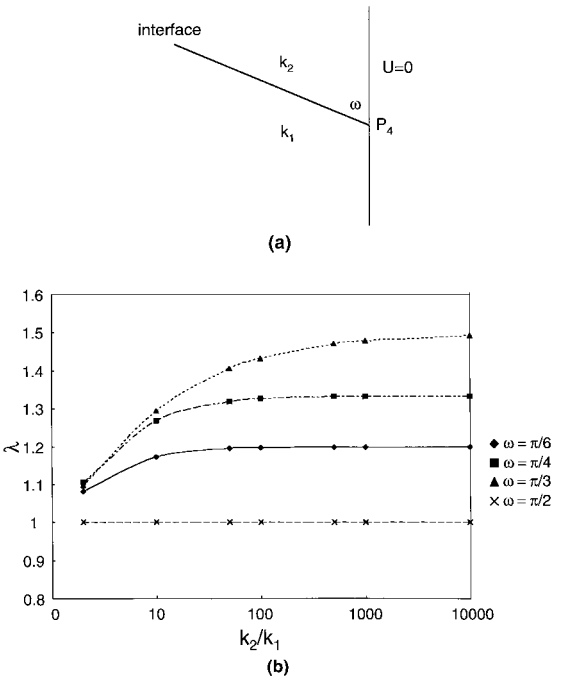

Fig. 14. (a) Schematic of a constituent solution for a model domain: solution for the structural eigenvalue in the potential field around singular point P_3 (see Fig. 9a, with boundary conditions as in Fig. 10a), and (b) values of the associated exponents for various values ω, over a range of volume fractions.

have associated singularities identical to point P_1, being independent of exterior boundary conditions as shown in Appendix B). Results for these points (given as P_4 only due to symmetry) are contained in Figs. 14 and 15, for the generalized boundary conditions of Fig. 10a and b, respectively. These results depend on the value of the potential at the edge ($\omega=0$ and $\xi=0$ in Figs. 14a and 15a, respectively). But, we can simply solve for the exponent associated with the singular point solution using general potential boundary condition $U=v$, then substitute $v=0$ and $v=-1$, respectively, for the two remaining cases. We obtain

$$
\begin{aligned}
&k_2 \sin(\pi\lambda_4/2)\cos(3\pi\lambda_4/2)\sin^2(\zeta\lambda_4+\pi\lambda_4/2)\\
&\quad-\frac{1}{2}k_2\sin(\pi\lambda_4/2)\sin(3\pi\lambda_4/2)\sin(2\zeta\lambda_4+\pi\lambda_4)\\
&\quad-k_2\cos(\pi\lambda_4/2)\sin(3\pi\lambda_4/2)\cos^2(\zeta\lambda_4+\pi\lambda_4/2)\\
&\quad-k_2 v\sin(3\pi\lambda_4/2)\cos^2(\zeta\lambda_4+\pi\lambda_4/2)\\
&\quad+\frac{1}{2}k_2\cos(3\pi\lambda_4/2)\cos(\pi\lambda_4/2)\sin(2\zeta\lambda_4+\pi\lambda_4)\\
&\quad+\frac{1}{2}k_2 v\cos(3\pi\lambda_4/2)\sin(2\zeta\lambda_4+\pi\lambda_4)\\
&\quad-k_1\cos(\pi\lambda_4/2)\sin(3\pi\lambda_4/2)\sin^2(\zeta\lambda_4+\pi\lambda_4/2)\\
&\quad+\frac{1}{2}k_1\sin(\pi\lambda_4/2)\sin(3\pi\lambda_4/2)\sin(2\zeta\lambda_4+\pi\lambda_4)\\
&\quad+k_1 v\sin(\pi\lambda_4/2)\\
&\quad-k_1 v\sin(3\pi\lambda_4/2)\sin^2(\zeta\lambda_4+\pi\lambda_4/2)\\
&\quad-\frac{1}{2}k_1\cos(3\pi\lambda_4/2)\cos(\pi\lambda_4/2)\sin(2\zeta\lambda_4+\pi\lambda_4)\\
&\quad+k_1\cos(3\pi\lambda_4/2)\sin(\pi\lambda_4/2)\cos^2(\zeta\lambda_4+\pi\lambda_4/2)\\
&\quad-\frac{1}{2}k_1 v\cos(3\pi\lambda_4/2)\sin(2\zeta\lambda_4+\pi\lambda_4)=0, \qquad (25)
\end{aligned}
$$

where the dummy angle $\zeta=\omega$, for $v=0$ (Fig. 14a, b) and $\zeta=\xi$, for $v=-1$ (Fig. 15a and b).

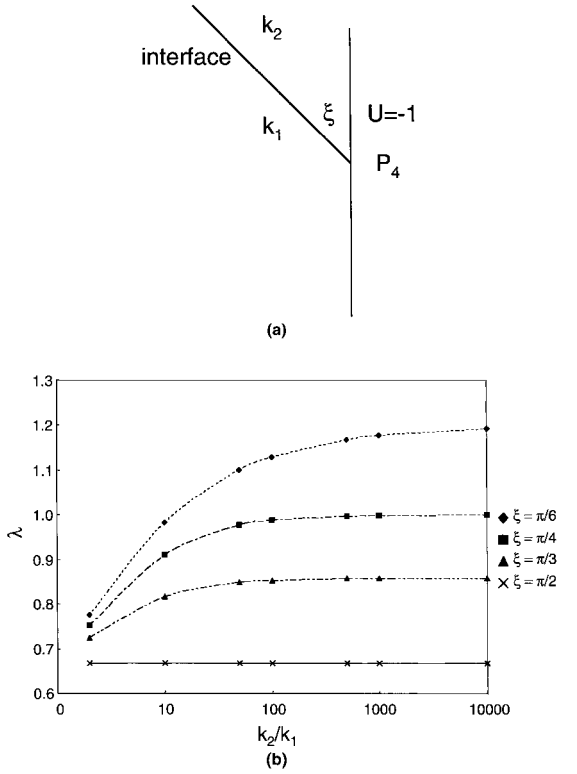

Fig. 15. (a) Schematic of a constituent solution for a model domain: solution for the structural eigenvalue in the potential field around singular point P_4 (see Fig. 9b, with boundary conditions as in Fig. 10b), and (b) values of the associated exponents for various values ξ, over a range of volume fractions.

With these singularities in hand, we can develop a strategy for solution of our own problem. Furthermore, we can comment on the strategy as it might compare with solution in domains with alternative boundary conditions or strengths of singularities.

3. Results and discussion

Using the two simulation approaches developed, along with derivations of solutions in generalized domains, we address four key issues: (1) the use of resistor network versus full-field solution, (2) scale effects in solution domains, (3) ability of network approaches to model experimentally-obtained conductivities and variances in conductivities, and (4) the development of numerical singularities in stochastic network analysis, and practical simulation ranges using the techniques described here. These issues are discussed in order. In all plots, data classified by contrast ($K_{\text{fiber}}/K_{\text{matrix}}$) indicate a solution via a FE (field) solution, per Section 2.2; if no contrast is given, data result from resistor network calculation, per Section 2.1.

3.1. 1D resistor networks versus elliptical inclusions

To reiterate, simulations using both high and medium contrast approaches are performed with two requirements in mind. The first requirement is to determine the degree of contrast which necessitates use of the more computationally intensive, low-contrast approach. The second requirement is to determine the benefit of moderate increase in "matrix" or electrolytic or active material in battery substrate, from a technological standpoint.

Degree of contrast and use of simplified approaches. Fig. 16 shows the dependence of normalized effective conductivity on volume fraction for several cases of contrast, spanning three orders of magnitude in the FE simulations ($K_{\text{fiber}}/K_{\text{matrix}} = 10 \rightarrow K_{\text{fiber}}/K_{\text{matrix}} = 1000$), against the result for the resistor network simulations ($K_{\text{fiber}}/K_{\text{matrix}} \rightarrow \infty$). Five simulations were performed for each of the averaged data shown. Beyond contrasts of around $K_{\text{fiber}}/K_{\text{matrix}} = 1000$, there is little difference ($\lesssim 1\%$) in results from the resistor network and FE simulations. Even in the range of $K_{\text{fiber}}/K_{\text{matrix}} = 100$, although the differences in calculated conductivities are moderately high as a percentage, there is little practical difference in view of the high variability in the generated microstructures, particularly at volume fractions less than 30%.

The greatest increase in conductivity (from the FE simulations) occurs between $K_{\text{fiber}}/K_{\text{matrix}} = 10$ and $K_{\text{fiber}}/K_{\text{matrix}} = 50$. This has significance for design of materials: although a 30-fold increase is possible at 30% volume fraction, by use of a material with a moderately conductive matrix phase ($K_{\text{fiber}}/K_{\text{matrix}} = 50$) versus a porous network ($K_{\text{fiber}}/K_{\text{matrix}} \rightarrow \infty$), order of magnitude gains are

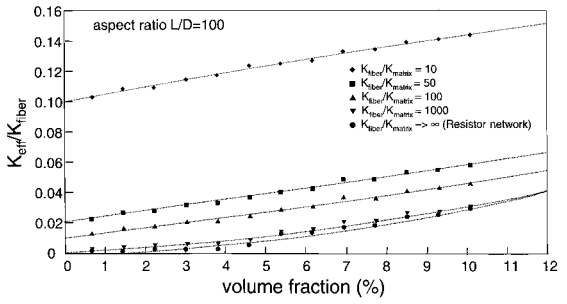

Fig. 16. Averaged values of simulations (five simulations for each condition) – normalized effective conductivity ratio ($K_{\text{eff}}/K_{\text{fiber}}$) versus volume fractions, for various material contrasts, for a uniform fiber orientation distribution.

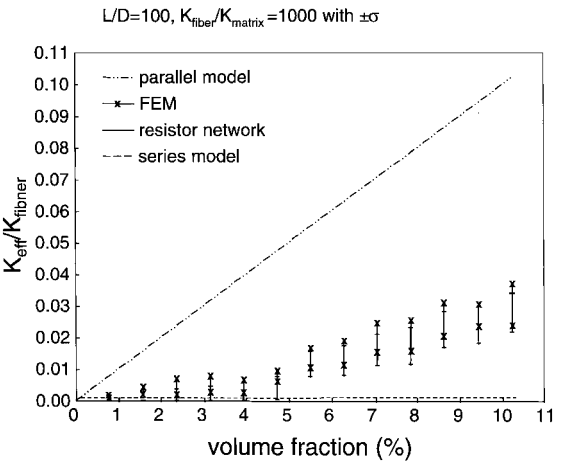

Fig. 17. Comparison among traditional bounds and simulations (shown $\pm 1\sigma$) for two simulation types (five simulations for each condition) – normalized effective conductivity ratio ($K_{\text{eff}}/K_{\text{fiber}}$) versus volume fractions, for $K_{\text{fiber}}/K_{\text{matrix}} = 1000$. Fibers' orientation are uniformly distributed.

not achieved until the conductivities themselves are of the same magnitude.

Comparison with rigorous bounds, and predicted variance. It is important to note that the simulations of Fig. 16 predict conductivities well below the prediction of the upper bound. Indeed, several micromechanics theories may be reduced for the case of zero conductivity in one-phase to develop deterministic predictions for the relation between effective conductivity and volume fraction of a single conductive phase; most fall relatively close to the upper bound (Cheng et al., 1999b). Comparison of Figs. 16 and 17 demonstrates this point; it can be seen that the more realistic stochastic simulations predict conductivities consistent with the upper bound for the high-contrast case (the parallel model, Eq. (2)) only when the conductivity of the two phases is of the same magnitude ($K_{\text{fiber}}/K_{\text{matrix}} = 10$). Thus, the stochastic construction of the materials plays a significant role in their effective properties, as it represents an extremely significant departure from idealized descriptions of microstructure. The effects of particle shape and other geometric descriptors are discussed below in greater detail.

We also wish to address the need for accurate prediction of variance in results. This aim differentiates this approach from classic work in effective properties in composite media, which typically seeks to deterministically predict average properties. Technologically, it is very important to be able to predict variability in reported conductivities for substrate material, since such measurements are an often-performed "proof test" of material suitability for use in batteries (Sastry et al., 1998b). Thus, it is very important to be able to distinguish high variability which arises simply because of the way that the material parameters are selected (i.e., the distributions of the microstructures in the material), and variability which arises due to defects or other problems in manufacturing of the material. Furthermore, one might wish to alter somewhat the material parameters selected, in order to reduce the expected material variability.

Fig. 17 shows good agreement in prediction of variance in properties using the two generation approaches described in Section 2, with a high-contrast case chosen ($K_{\text{fiber}}/K_{\text{matrix}} = 1000$) for purposes of reasonable comparison. This indicates that although the model microstructures are certainly different (ellipses versus 1D fibers, with the latter being periodic), they offer similar predictions of both average properties and variance and properties for the same initial network parameters. Both predictions also lie well below the upper bound, even in light of the significant variances, which is discussed later in greater detail.

Influence of geometric parameters. Figs. 18–20 show the results of simulations on microstructures

containing several types of conductive fiber shapes. These results can assist development of some practical guidelines in selection of battery materials, and are performed in realistic regimes for substrate materials.

Fig. 18 shows averaged simulations' predictions of normalized effective conductivity for two "fiber" types: the first has an aspect ratio (L/D) of 100, with a single-valued staple length (in simulation terms, the original length of a fiber "placed" in a model domain) for all fibers of 1; the second has aspect ratio and staple length of 50 and 1, respectively. Since the staple lengths in both cases are unity (i.e., the simulation window size is identical to the input fiber length) the diameter of these two particle types are unequal – 0.01 and 0.02, respectively. At lower volume fractions (2–10%), we observe a significant advantage in use of high aspect-ratio fibers. Indeed, the greatest advantage is achieved in volume fractions between ~6–9%. These values are of technological interest, as discussed later.

Thus, this comparison of particle types quantifies the effect of connectivity in this class of fibrous networks. With no additional conductive mass, a doubling of staple length and halving of diameter in fibers used can produce a 50-fold improvement in conductivity (5% volume fraction). This advantage is evident even at low volume fractions, despite the significant volumes of "trimmed" (nonconductive ends not spanning at least two bonds) material. Connectivity (i.e., bond density) is significantly improved for the higher aspect ratio particles, even though each of the comparisons has the same number of particles and volume fraction.

Effective conductivity and variance in conductivity are both relatively insensitive to alteration of staple length in terms of the selected unit cell size, in the regime relevant to substrate materials ($L/L_u = 1.0$ versus $L/L_u = 1.5$; discussed in greater detail by Cheng et al., 1999b). This can be verified by comparison of Figs. 18 and 19, for average values. The variances in simulated effective conductivities, however, are strongly influenced by fiber shape. Not only can significant improvements in conductivity be achieved with modest changes in fiber geometry, but variances can be much better controlled. Fig. 19a and b illustrate this effect:

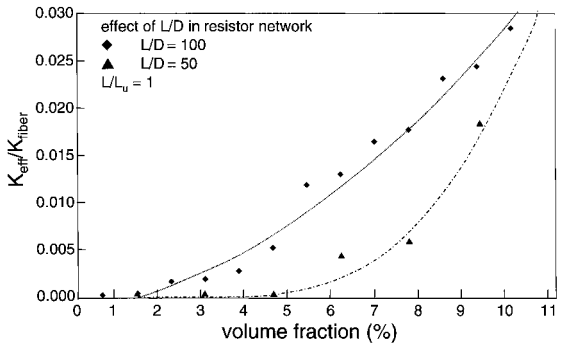

Fig. 18. Effect of aspect ratio on average conductivity in resistor networks. Fibers' orientations are uniformly distributed (20 simulations for each condition).

the lower aspect ratio materials often fail to produce networks which span the simulated domain (note the zero-valued lower 1σ-bound for volume fractions below 60% in Fig. 19a), even at high volume fractions. For practical purposes, this implies that (1) particles must be continuously redeposited onto the network being produced in order to manufacture continuous sheets of material comprised of low-aspect ratio particles, and (2) even when an iterative scheme is used to assure production of a continuous sheet of material, high variability is likely when testing at a scale within an order of magnitude or so of the staple length. By contrast, use of long fibers (Fig. 19b) can be expected to produce materials of much higher conductivity, with small variances even at very small testing scales.

3.2. Scale effects in solution domains

In simulations of heterogeneous domains, two issues pertaining to scale must be addressed. The first is determination of the size of the simulation "window" (model domain) relative to some characteristic particle or part of the microstructure. The second is determination of number of data (i.e., simulations) required to get stable, reproducible results at a particular scale. In simulations, the cost involved (as well as whether convergent solutions are even attainable) is also an issue. For these reasons, we wish to identify the smallest scales in simulations at which meaningful solutions

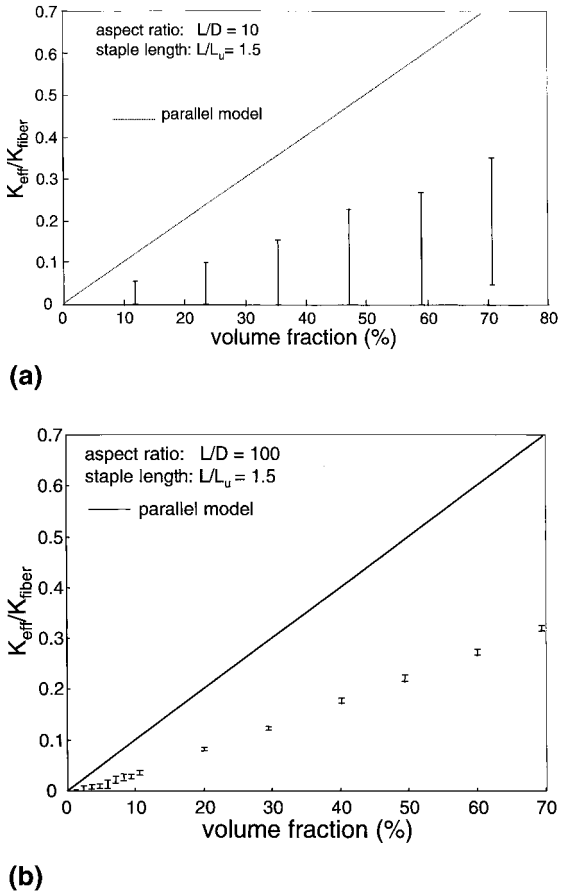

Fig. 19. Effective conductivity (including variance in conductivity shown as $\pm 1\sigma$ error bars), versus volume fraction of conductor, for two aspect ratios. Fibers' orientations are uniformly distributed (20 simulations for each condition).

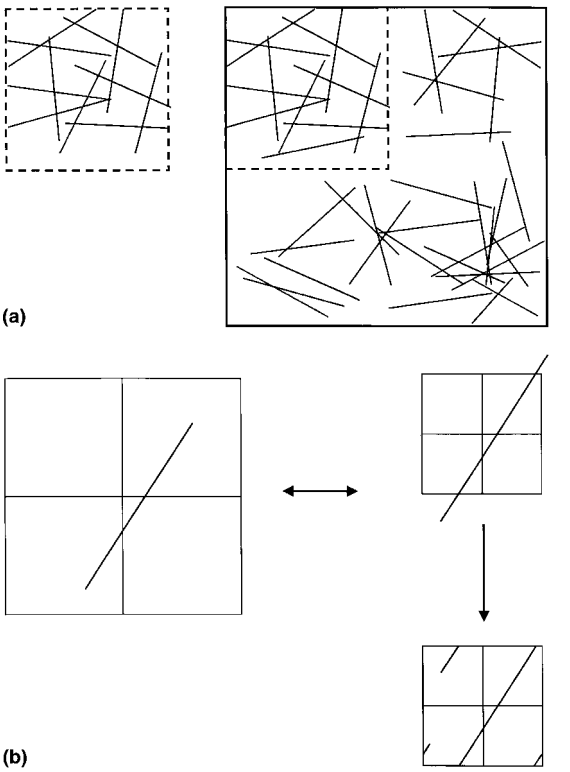

Fig. 20. Schematics showing the effect of scale (20 simulations for each condition), including (a) selection of characteristic domain, and (b) consequence in enforcing periodicity (selection of staple length for simulation).

can be obtained (and, conversely, the largest scales that can be practically examined), and corresponding regimes of experimental scales to validate the simulations. Fig. 20 illustrates two related questions in selection of scale.

We must select a "window size" (Fig. 20a) for a simulation. We can scale this as the fiber diameter, fiber staple length, or iteratively, as some other parameter (e.g., segment length, etc.). Experimentally, this is equivalent to selection of the distance between probes placed on a sheet of material to determine its conductivity.

Selection of the window size has important ramifications in use of the network reduction approach (with the resistor network analysis in cases of high contrast). As shown in Fig. 20b, selection of a small window size assures that the generated fibers (whose centerpoints lie in the unit cell) will be truncated when periodicity is enforced, producing smaller segments in the unit cell (though preserving the orientation distribution selected for all segments). This in turn affects connectivity in the unit cell. The central question is whether this network generation approach for producing periodic unit cells adequately captures the behavior over a reasonably wide range of sizes. Importantly, when the window size is reduced (preserving the same staple length) the ratio between staple length and window size (L/L_u) increases.

Figs. 21 and 22 address these points. In each figure, normalized resistivity, rather than conductivity, is plotted, and each ordinate is plotted using

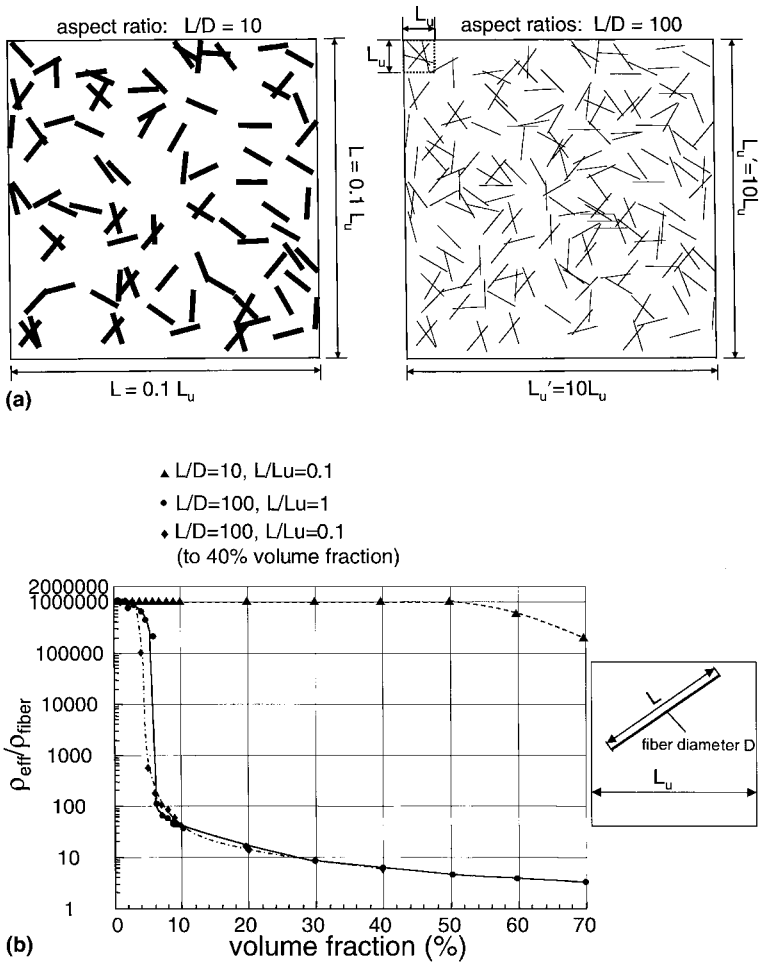

Fig. 21. (a) Schematic of model domains, for (b) normalized effective resistivity ratio (logarithmic) for several combinations of aspect ratio and window size (staple length), versus volume fraction of conductor (20 simulations for each condition).

a logarithmic scale, so that all of the data can be displayed. In each plot, three materials are simulated, to investigate two effects (shown schematically in Fig. 21a):

1. The effect of increasing the window size (scale effect) on two networks with geometrically similar fibers. This can be assessed by comparison of the cases $\{L/D = 100,\ L/L_u = 1\}$ and $\{L/D = 100, L/L_u = 0.1\}$.
2. The effect of increasing staple length of fibers of the same diameter. This can be assessed by comparison of the cases $\{L/D = 10, L/L_u = 0.1\}$ and $\{L/D = 100, L/L_u = 1\}$. In both cases, $D = 0.01$ for the unit cell.

Scale effect ("window size") and staple effect are investigated here simultaneously to allow comparison of material geometry with scale of simulation.

Fig. 21 demonstrates that there is little scale effect on mean properties (see comment 1 above). While we generally expect to see convergence at the mean for all scales in effective properties for a sufficient number of data, we also expect to see differences in variances at each scale. We observe in these materials (for five simulations at each condition), that there was significant "noise" in coefficient of variation in the simulated data at low volume fractions, but that the coefficients of

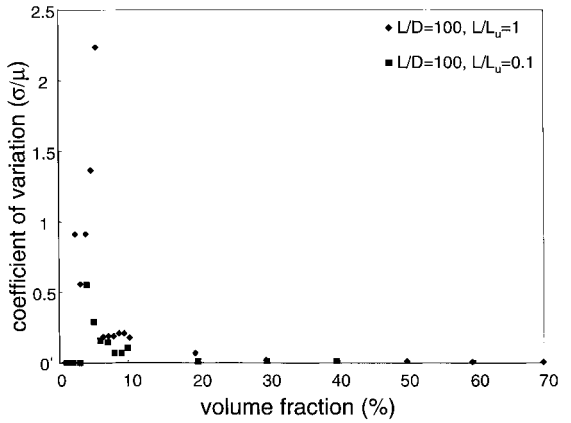

Fig. 22. Average coefficients of variation (μ/σ) for the simulation data of Fig. 21 (20 simulations for each condition). Plots are shown for the two cases used for assessment of the effect of scale effect ($\{L/D = 100,\ L/L_u = 1\}$ and $\{L/D = 100,\ L/L_u = 0.1\}$).

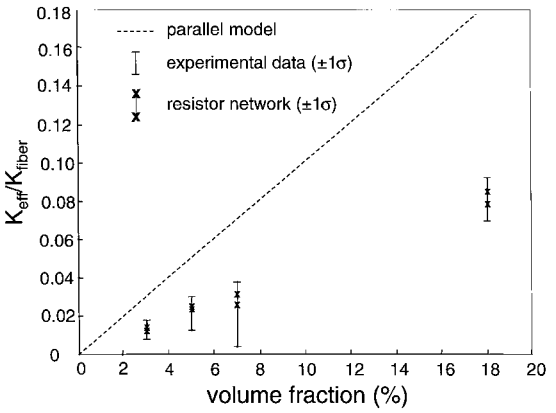

Fig. 23. Comparison of experimental normalized conductivity ratios versus simulation (five simulations, each condition), using the resistor network approach, versus volume fraction of conductor.

variation converged for the two size scales at moderate material volume fraction (~30%).

The very strong effect of staple length in conduction can also be seen in Fig. 21 (see comment 2 above), with networks comprised of low aspect ratio fibers having resistivities several orders of magnitude higher than those networks comprised of fibers with high aspect ratio. This confirms the earlier result described by Fig. 19, for a differently scaled domains, but with variation in staple length by the same amount (×10).

3.3. Experimental validation

Experiments were performed to determine the resistivity (which can be inverted, for conductivity) of various battery substrate materials. Table 1 gives the material parameters for each of the four materials, whose volume fractions ranges from 3% to 18%. Simulations were performed using the resistor network approach. Conductivities were very well predicted by the simulations, and simulations' variances were, perhaps somewhat surprisingly, higher than those measured experimentally, though in reasonable agreement (Fig. 23). In this case, particle mass was modeled as fiber mass, since particles were of similar diameter.

3.4. Numerical singularities and practical simulation ranges

Component solutions are given for the singular points of interest in stochastic fibrous networks, in Section 2. These singular points were identified from three model domains, pictured in Fig. 9.

Table 1
Material properties of Ni/MH battery substrates tested

Material type	Thickness	Content	Fiber D	Fiber staple length	Vol.% nickel
Fibrex (001–008)	0.03″ (0.075 cm)	97% pure nickel, 3% contaminant; 50/50 blend fiber/powder	~30 μm	0.25–0.5′ (~0.64–1.3 cm)	~18%
Fibrex (001–028)	0.08″ (0.20 cm)	97% pure nickel, 3% contaminant; 50/50 blend fiber/powder	~30 μm	0.25–0.5′ (~0.64–1.3 cm)	~7%
AFS (001–009)	0.65″ (0.165 cm)	99% pure nickel; 50/50 blend fiber/powder	~20 μm	0.5–0.75′ (~1.3–1.9 cm)	~3%
AFS (001–029)	0.06″ (0.15 cm)	99% pure nickel; 50/50 blend fiber/powder	~20 μm	0.5–0.75′ (~1.3–1.9 cm)	~5%

Numerical solution of Laplace's equation was carried out for the two sets of boundary conditions described graphically in Fig. 10 (with those in Fig. 10a suggested as a test of convergence by Oh and Babuska (1995), and the periodic boundary conditions in of Fig. 10b are used in the present work for solution for effective conductivity as in Eq. (6)). All computations were performed using a Sun Ultra I workstation with a 140 MHz processor, using a commercial finite element code (Maxwell 2D), with triangular elements.

Fig. 24 gives the dimensions for the simulation domains. Table 2 gives the number of elements required for solution (if convergence is achievable) for all domains, angles and boundary conditions. Two criteria were used to measure convergence for these simulations. First, energy error was examined. In this test, the satisfaction of the governing equation (Laplace's equation) is evaluated in each phase, for each adaptive step. Second, iteration error was examined, comparing the percent energy change between the last two adaptive solutions. Only when both errors fall below a target error value 0.1%, does the adaptive solution process stop. In a number of cases, triangular element meshes failed to produce convergent results (denoted "N" in Table 2).

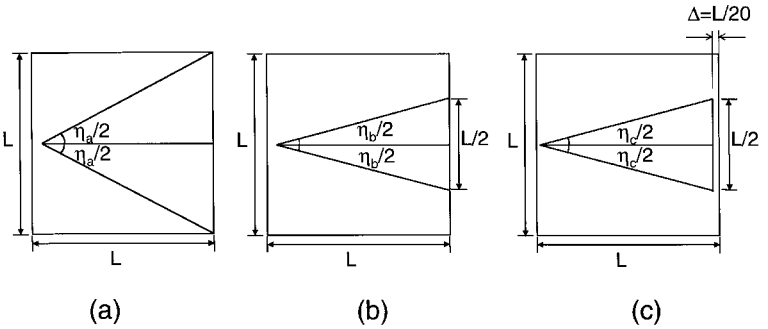

Fig. 24. Three specific domains investigated (dimensions as shown), to determine the magnitude of the singularities present in solution of Laplace's equation, (a–c) modeled on Fig. 9a–c respectively. Results on convergence when studied with boundary conditions of Fig. 10a and b are given in Table 1.

Table 2
Comparison of convergence in solution of Laplace's equation for microstructures shown in Fig. 9, with boundary conditions shown in Fig. 10. N indicates no convergence. 5% mesh refinement per pass was used in all simulations, with triangular elements

Boundary condition	Unit geometry		
	Fig. 24a	Fig. 24b	Fig. 24c
Fig. 10a		$\eta_b = \pi/6 - N$	$\eta_c = \pi/6 - N$
	$\eta_a = \pi/3 - N$	$\eta_b = \pi/4 - N$	$\eta_c = \pi/4 - N$
	$\eta_a = \pi/2 - N$	$\eta_b = \pi/3 - N$	$\eta_c = \pi/3 - N$
	$\eta_a = 2\pi/3 - N$	$\eta_b = \pi/2 - N$	$\eta_c = \pi/2 - N$
	$\eta_a = 3\pi/4 - N$	$\eta_b = 2\pi/3 - N$	$\eta_c = 2\pi/3 - N$
	$\eta_a = 5\pi/6 - N$	$\eta_b = 3\pi/4 - N$	$\eta_c = 3\pi/4 - N$
		$\eta_b = 5\pi/6 - N$	$\eta_c = 5\pi/6 - N$
Fig. 10b		$\eta_b = \pi/6 - 14$	$\eta_c = \pi/6 - 102$
	$\eta_a = \pi/3 - N$	$\eta_b = \pi/4 - 155$	$\eta_c = \pi/4 - 75$
	$\eta_a = \pi/2 - N$	$\eta_b = \pi/3 - 151$	$\eta_c = \pi/3 - 86$
	$\eta_a = 2\pi/3 - N$	$\eta_b = \pi/2 - 191$	$\eta_c = \pi/2 - 119$
	$\eta_a = 3\pi/4 - N$	$\eta_b = 2\pi/3 - 168$	$\eta_c = 2\pi/3 - 116$
	$\eta_a = 5\pi/6 - N$	$\eta_b = 3\pi/4 - 214$	$\eta_c = 3\pi/4 - 152$
		$\eta_b = 5\pi/6 - 199$	$\eta_c = 5\pi/6 - 180$

Comparison of Table 2, and Figs. 10 and 24 demonstrate that, as expected, the solution domain of Fig. 24a and the boundary conditions of Fig. 10a present significant numerical challenges for simple elements. Figs. 12 and 13 demonstrate the severity of the P_3 singularity of Fig. 9a (and Fig. 24a). This singularity, the strongest calculated for the five cases examined, is sufficiently strong, however, to prevent convergence in both boundary condition applications.

The singularities arising in the other domains of interest (Fig. 24b, c) for our boundary conditions (Fig. 10b) were not sufficiently strong to prevent solution despite use of simple elements with mesh refinement only.

4. Conclusions and future work

Simulations have suggested that in a range of physically realistic parameters for materials used in battery substrates, the effects of scale are small. For these materials, practical stochastic finite element solutions are fully capable of predicting both effective conductivity and variance in conductivity.

Results suggest that higher staple lengths are key in developing superior materials. Because of the relatively high threshold for improvement of conductivity with increase in a second phase's conductivity, strategies including improving matrix conductivity do not seem promising. Although scale effects in simulations are a concern for materials in which practical experiments cannot be carried out on volumes within a few orders of magnitude of a characteristic scale in the material, scale effects do not appear to hinder solution in the cases examined here. Furthermore, although variance can be reasonably expected to increase dramatically with scale, the large simulations performed here did not encounter significant difficulty, since the simulation scale and material scale are within $\sim$2 orders of magnitude.

The resistor network approach appears to be an accurate tool for analysis of multiphase fiber structures with relatively high contrasts. The stochastic finite element approach appears to perform well for the high contrast cases examined, giving robust and consistent support to statistical findings in the resistor network approach. Numerical difficulties commonly encountered with such models were examined here in some detail, but despite some reasonably strong singularities, we show that the combination of the model domain and boundary conditions in this application allows solution with a simple approach (mesh refinement using simple elements). The greatest numerical challenges appear to arise at interfaces between flux and potential boundary conditions. Future work will attempt to use smoothing approaches to relax these singularities enough to allow investigation of denser and larger structures.

Future work will also address the effects of moderate alignment, and greater (realistic) variability in fiber characteristics (diameter, staple length). For larger simulations performed in the course of this study, some convergence issues have arisen: future work will attempt to explain these difficulties (i.e., identify further internal microstructures which cause them) and suggest strategies for solution.

Acknowledgements

The authors gratefully acknowledge the support of Department of Energy and the Lawrence Berkeley Laboratories, under the ETR Program. Additional support from a National Science Foundation PECASE grant is also gratefully acknowledged. Helpful discussions with Professor Peter Smereka (Mathematics Department, University of Michigan) on singularities in solution of Laplace's equation were also greatly appreciated.

Appendix A. Solution of Laplace's equation in a heterogeneous two dimensional domain containing *M* singularities

Laplace's equation in two dimensional domain may be written

$$\Delta U = 0 \tag{A.1}$$

or, in expanded form in Cartesian or polar coordinates, respectively,

$$\frac{\partial^2 U}{\partial^2 x}+\frac{\partial^2 U}{\partial^2 y}=0 \tag{A.2}$$

and

$$\frac{\partial^2 U}{\partial^2 r}+\frac{1}{r}\frac{\partial U}{\partial r}+\frac{1}{r^2}\frac{\partial^2 U}{\partial^2 \theta}=0. \tag{A.3}$$

In a domain containing M singularities, we can write an exact solution of the latter problem in terms of (r,θ) may be written

$$U_{\mathrm{ex}}=\sum_{q=1}^{M}\sum_{j=1}^{\infty}k_{jq}r_q^{\lambda_{jq}}f_{jq}(\theta_q). \tag{A.4}$$

Substitution into the governing equation yields

$$\frac{\partial^2 U_q}{\partial^2 r_q}+\frac{1}{r_q}\frac{\partial U_q}{\partial r_q}+\frac{1}{r_q^2}\frac{\partial^2 U_q}{\partial^2 \theta_q}=0, \tag{A.5}$$

where the individual terms are given by

$$\frac{\partial^2 U_q}{\partial^2 r_q}=\sum_{j=1}^{\infty}\lambda_{jq}(\lambda_{jq}-1)k_{jq}r_q^{\lambda_{jq}-2}f_{jq}(\theta_q), \tag{A.6}$$

$$\frac{1}{r_q^2}\frac{\partial^2 U_q}{\partial^2 \theta_q}=\sum_{j=1}^{\infty}k_{jq}r_q^{\lambda_{jq}-2}f''_{jq}(\theta_q), \tag{A.7}$$

$$\frac{1}{r_q}\frac{\partial U_q}{\partial r_q}=\sum_{j=1}^{\infty}\lambda_{jq}k_{jq}r_q^{\lambda_{jq}-2}f_{jq}(\theta_q). \tag{A.8}$$

Combination of terms yields

$$\sum_{j=1}^{\infty}k_{jq}r_q^{\lambda_{jq}-2}\left[\lambda_{jq}^2 f_{jq}(\theta_q)+f''_{jq}(\theta_q)\right]=0 \tag{A.9}$$

and therefore

$$\lambda_{jq}^2 f_{jq}(\theta_q)+f''_{jq}(\theta_q)=0. \tag{A.10}$$

Finally solving for terms f, we find

$$f_{jq}(\theta_q)=a_{jq}\cos(\lambda_{jq}\theta_q)+b_{jq}\sin(\lambda_{jq}\theta_q) \tag{A.11}$$

which allows final expression of U as

$$U_q=\sum_{j=1}^{\infty}k_{jq}r_q^{\lambda_{jq}}\left[a_{jq}\cos(\lambda_{jq}\theta_q)+b_{jq}\sin(\lambda_{jq}\theta_q)\right]. \tag{A.12}$$

Appendix B. Solution of Laplace's equation in a two-phase domain containing a corner singularity

The intensity of singularity of P_1 (Fig. 11a) is determined as follows. Interface boundary conditions are applied at a circle of arbitrary radius around point P_1. We require equal potential for $\theta=0$ and $\theta=2\pi$ as

$$\cos(\lambda_1 0)+B\sin(\lambda_1 0)=C\cos(\lambda_1 2\pi)+D\sin(\lambda_1 2\pi). \tag{B.1}$$

We also have at the other interface $\theta=\alpha$,

$$\cos(\lambda_1\alpha)+B\sin(\lambda_1\alpha)=C\cos(\lambda_1\alpha)+D\sin(\lambda_1\alpha). \tag{B.2}$$

We further require equal flux along the interface at $\theta=0$ and $\theta=2\pi$, as

$$k_1\lambda_1[-\sin(\lambda_1 0)+B\cos(\lambda_1 0)]=k_2\lambda_1[-C\sin(\lambda_1 2\pi)+D\cos(\lambda_1 2\pi)] \tag{B.3}$$

and along the other interface along $\theta=\alpha$, we have

$$k_1\lambda_1[-\sin(\lambda_1\alpha)+B\cos(\lambda_1\alpha)]=k_2\lambda_1[-C\sin(\lambda_1\alpha)+D\cos(\lambda_1\alpha)]. \tag{B.4}$$

Solving these four equations simultaneously, we obtain λ_1. We can write the general solution for the exponent as

$$\begin{aligned}&k_2k_1\sin(2\lambda_1\alpha)\sin(2\lambda_1\pi)-2k_2k_1\cos^2(\lambda_1\alpha)\cos(2\lambda_1\pi)\\&+\frac{1}{2}k_2^2\sin(2\lambda_1\alpha)\sin(2\lambda_1\pi)+2k_2k_1-k_2^2\cos(2\lambda_1\pi)+k_2^2\cos^2(\lambda_1\alpha)\cos(2\lambda_1\pi)\\&+\frac{1}{2}k_1^2\sin(2\lambda_1\alpha)\sin(2\lambda_1\pi)-k_1^2\cos(2\lambda_1\pi)+k_1^2\cos(2\lambda_1\pi)\cos^2(\lambda_1\alpha)=0.\end{aligned} \tag{B.5}$$

Thus, the intensity of the singularity at point P_1 is purely determined by the material contrast and geometry, and therefore the boundary conditions applied (e.g., flux versus potential) are not a factor.

References

Babuska, I., Oh, H.S., 1990. The p-version of the finite element method for domains with corners and for infinite domains. Numer. Methods PDEs 6, 371–392.

Babuska, I., Andersson, B., Guo, B., Melenk, J.M., Oh, H.S., 1996. Finite element method for solving problems with singular solutions. J. Comp. Appl. Math. 74 (1/2), 51–70.

Borcea, L., Papanicolaou, G.C., 1997. A hybrid numerical method for high contrast conductivity problems. J. Comp. Appl. Math. 87, 61–77.

Cheng, X., Wang, C.W., Sastry, A.M., Choi, S.B., 1999a. Investigation of failure processes in porous battery substrates: Part II – simulation results and comparisons. ASME J. Engrg. Materials Tech. (to be published, October 1999).

Cheng, X., Sastry, A.M., Layton, B.E., 1999b. Transport in stochastic fibrous networks. ASME J. Engrg. Materials and Tech. (in preparation).

Ferrando, W.A., Lee, W.W., Sutula, R.A., 1984. A lightweight nickel composite electrode I: concept and feasibility. J. Power Sources 12, 249–265.

Hashin, Z., Shtrikman, S., 1962. A variational approach to the theory of the effective magnetic permeability of multiphase materials. J. Appl. Phys. 33, 3125–3131.

Kirkpatrick, S., 1973. Percolation and conduction. Rev. Modern. Phys. 45 (4), 574–588.

Mardia, K.V., 1972. Statistics of Directional Data. Academic Press, London, New York.

McLachlan, D.S., 1988. Measurement and analysis of a model dual-conductivity medium using a generalized effective-medium theory. J. Phys. C: Solid State Phys. 21, 1521–1522.

McLachlan, D.S., Blaskeiwicz, M., Newnham, R.E., 1990. Electrical resistivity of composites. J. Amer. Ceram. Soc. 73 (8), 2187–2203.

Meredith, R.E., Tobias, C.W., 1962. II. Conduction in heterogeneous systems. Advances in Electrochemistry and Electrochemical Engineering, Intersciense, New York, pp. 15–47.

Oh, H.S., Babuska, I, 1992. The p-version of the finite element method for the elliptic boundary value problems with interfaces. Comp. Methods App. Mech. Engrg. 97, 211–231.

Oh, H.S., Babuska, I., 1995. The method of Auxiliary Mapping for the finite element solutions of elasticity problems containing singularities. J. Comp. Phys. 121, 193–212.

Ostoja-Starzewski, M., Sheng, P.Y., Jasiuk, I., 1994. Influence of random geometry on effective properties and damage formation in composite materials. J. Engrg. Materials Tech. 116, 384–391.

Ostoja-Starzewski, M., Sheng, P.Y., Alzebdeh, K., 1996. Spring network models in elasticity and fracture of composites and polycrystals. Comp. Materials Sci. 7, 82–93.

Sastry, A.M., Cheng, X., Wang, C.W., 1998a. Mechanics of stochastic fibrous networks. J. Thermoplast. Compos. Mater. 11, 288–296.

Sastry, A.M., Cheng, X., Choi, S.B., 1998b. Damage in composite Ni/MH positive electrodes. ASME J. Engrg. Materials Tech. 120, 280–283.

Schulgasser, K., 1985. Fiber orientation in machine-made paper. J. Materials Sci. 20, 859–866.

Tatarchuk, B.J., 1994. Composite fiber structures for catalysts and electrodes. J. Power Sources 47, 297–302.

Wang, C., Cheng, X., Sastry, A.M., Choi, S.B., 1999. Investigation of failure processes in porous battery substrates: Part I – experimental findings. ASME J. Engrg. Materials Tech. (to be published, October 1999).